TU Delft

Delft University of Technology

The effect of micromechanical stresses on vacancy formation and stress-driven mass-transport in polycrystalline Fe–Au alloy

Hussein, Abdelrahman; van der Zwaag, Sybrand; Kim, Byungki

DOI
10.1016/j.matchemphys.2024.128878

Publication date
2024

Document Version
Final published version

Published in
Materials Chemistry and Physics

Citation (APA)
Hussein, A., van der Zwaag, S., & Kim, B. (2024). The effect of micromechanical stresses on vacancy formation and stress-driven mass-transport in polycrystalline Fe–Au alloy. *Materials Chemistry and Physics*, *315*, Article 128878. https://doi.org/10.1016/j.matchemphys.2024.128878

Important note
To cite this publication, please use the final published version (if applicable).
Please check the document version above.

Copyright
Other than for strictly personal use, it is not permitted to download, forward or distribute the text or part of it, without the consent of the author(s) and/or copyright holder(s), unless the work is under an open content license such as Creative Commons.

Takedown policy
Please contact us and provide details if you believe this document breaches copyrights.
We will remove access to the work immediately and investigate your claim.

This work is downloaded from Delft University of Technology.
For technical reasons the number of authors shown on this cover page is limited to a maximum of 10.

Materials Chemistry and Physics 315 (2024) 128878

Contents lists available at ScienceDirect

Materials Chemistry and Physics

journal homepage: www.elsevier.com/locate/matchemphys

Full length article

The effect of micromechanical stresses on vacancy formation and stress-driven mass-transport in polycrystalline Fe–Au alloy

Abdelrahman Hussein [a,b], Sybrand van der Zwaag [d], Byungki Kim [b,c,*]

[a] Department of Materials, Textiles and Chemical Engineering, Ghent University, Technologiepark 46, B-9052 Ghent, Belgium
[b] School of Mechatronics Engineering, Korea University of Technology and Education, Republic of Korea
[c] Future Convergence Engineering, Korea University of Technology and Education, Cheonan, Chungnam 31253, Republic of Korea
[d] Faculty of Aerospace Engineering, Delft University of Technology, The Netherlands

GRAPHICAL ABSTRACT

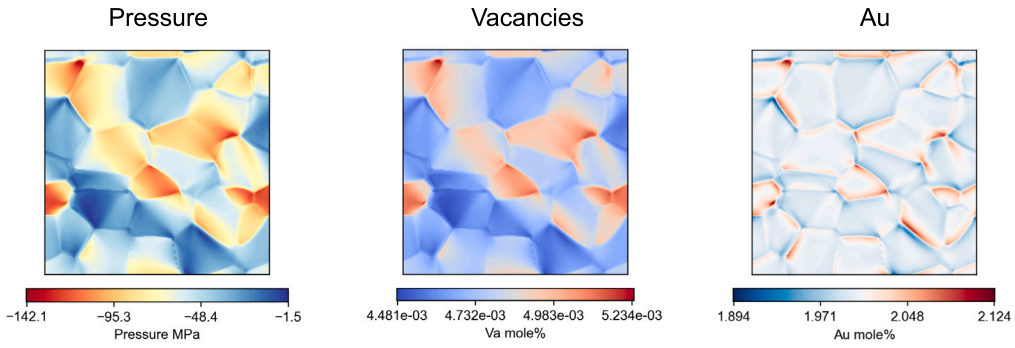

HIGHLIGHTS

- A model linking binary diffusion with stresses is presented for Fe–Au system.
- Vacancies have maximum concentration at regions with high tensile pressure.
- Au gets depleted from less tensile regions towards more tensile ones.
- Interaction of stresses, Va and Au on void growth and self-healing is presented.

ARTICLE INFO

Keywords:
Creep-voids
Self-healing
CALPHAD
Crystal plasticity
Cross diffusion
Vacancies

ABSTRACT

In recent years, a new class of super saturated binary and ternary alloys have demonstrated the ability for the self-healing of creep-induced voids formed at the grain boundaries. However, a clear understanding of the parameters affecting the self-healing mechanism is still not yet complete. One of the main challenges is understanding the effect of microstructure and micromechanical stresses on the redistribution of the healing-solute and vacancies. To this end, we address this issue using a CALPHAD-informed diffusion model coupled with crystal plasticity. In principle, the approach is general and can be used for any binary Fe–X alloy, but in this work Fe–Au binary system is used since it experimentally showed the best healing efficiency. First, we present a multicomponent diffusion model considering cross and stress-driven diffusion. The effect of stress was also considered on the equilibrium vacancy concentration. To investigate the effect of the micromechanical stresses, a representative volume element (RVE) was obtained using the phase-field method. The results showed that the maximum vacancy concentration is at the grain boundaries (GBs) with the highest hydrostatic tensile

* Corresponding author at: School of Mechatronics Engineering, Korea University of Technology and Education, Republic of Korea.
E-mail addresses: abdelrahman.hussein@ugent.be (A. Hussein), S.vanderZwaag@tudelft.nl (S. van der Zwaag), byungki.kim@koretech.ac.kr (B. Kim).

https://doi.org/10.1016/j.matchemphys.2024.128878
Received 31 July 2023; Received in revised form 14 December 2023; Accepted 31 December 2023
Available online 5 January 2024
0254-0584/© 2024 Elsevier B.V. All rights reserved.

stresses. These were also the regions of the highest Au enrichment. A crucial factor to achieve this is the high diffusivity of Au compared to the Fe matrix. Increasing the stresses, lead to an increase both in vacancy and Au concentration. The accompanying increased stress triaxiality is suggested to be the reason for the reduced self-healing efficiency observed in previous experimental studies.

1. Introduction

Creep is one of the primary damage mechanisms that affect metals subjected to prolonged loading at high temperatures ($T > 0.4T_{\text{melt}}$) [1]. One of the underlying mechanisms of creep-damage is void growth and coalescing [2,3] at grain boundaries (GBs), especially those perpendicular to the tensile loading direction [4,5], leading to micro-crack formation and rupture [6]. The most common strategies to enhance creep resistance include solid solution strengthening [7], precipitation hardening [8] and microstructure optimization [9,10]. However, these strategies become ineffective once irreversible void formation takes place, and thus, consequent growth, coalescence and rupture become inevitable.

A novel and promising methodology to mitigate this mechanism is autonomous self-healing in supersaturated alloys [11], i.e. the filling of crack-initiating sites without an external input. Indeed, self-healing has been reported for different types of materials including polymers, metals and ceramics [12–16]. In metallic alloys, the mechanism of self-healing is mostly based on solid-state diffusion, where the healing agent (solute atoms) diffuses and preferentially precipitate at open-volume defects [17]. The creep-damage self-healing has been shown to work for several model Fe-based binary alloys including Fe–Cu [18], Fe–Au [18,19], Fe–Mo [20], Fe–W [21] as well as ternary Fe–3Au–4 W [22,23]. The underlying mechanism is that a super-saturated solute will preferentially nucleate at open-volume defects like voids and subsequently fill them by precipitation growth. The filling of the pores does not only remove the voids and the accompanying stress concentration, but also reverses the vacancy flux away from to damage site [24]. Van Dijk and Van der Zwaag [17] summarized the essential factors for a successful self-healing solute: (i) the solute should be in a supersaturated state to develop a large driving force for precipitation, (ii) The precipitation should be preferential at the voids, thus, solute atomic radius should be larger than the solvent such that nucleation is suppressed in the matrix and be allowed only in open-volume defects like voids, (iii) the solute atom should have larger diffusivity than the self diffusion of the solvent.

Among the aforementioned solutes in Fe based alloys, Au shows the most effective *site-selectivity*, and thus, self-healing. This is attributed to the large atomic radius of Au compared to Fe, which impedes Au nucleation in Fe defect-free matrix due to large strain–energy. Furthermore, migrating Au atoms will not be trapped by other solute atoms forming immobile internal precipitates. And finally, the diffusion of Au is confirmed to be faster than the self diffusion of Fe [25,26].

Several efforts have been made to elucidate the factors affecting the self-healing efficiency. This included microstructure, competition between void growth and healing, effect of external loading and void and precipitate morphology [18,19,27–29]. In order to provide a theoretical framework for the competition of void growth and self-healing, several studies based on Fickian diffusion [24,30,31] in a simplified model of a bicrystal with a void located at the center of the grain boundary were presented. Despite the useful information provided by these models, they were based on a single component diffusion and did not provide the effect of cross diffusion between the solute and the solvent [32]. Furthermore, the effect of stresses [33–35] was not considered, and thus, the subsequent effect of complex microstructures and the resulting micromechanical heterogeneities [36] on stress-driven diffusion.

In this work, we investigate the effect of stresses and cross diffusion in Fe–Au system, since it has shown the most efficient self-healing ability as it best meets the physical criteria for self-healing. First, we summarize the multicomponent diffusion system of equations, while accounting for the effect of stresses. This allows for investigating the effect of diffusivity of Au on the cross diffusion, i.e. how Au flux is affected by Fe concentration gradient and vice versa. The diffusion coefficients were calculated using CALPHAD based thermodynamic database, paving the way for investigating technologically relevant binary and multicomponent alloys. To investigate the role of micromechanical stresses, we used a representative volume element (RVE) generated by the phase-field method. This also allowed for evaluating the effect of stresses on equilibrium thermal vacancy concentration. It should be pointed here that we only considered one-way coupling of stress and diffusion, i.e. how stress affects the diffusion flux. The two-way coupling will be investigated in future studies. Additionally, damage, i.e. void nucleation and growth, as well as healing, i.e. precipitation of Au in open volume voids is not evaluated in this work. Therefore, we only investigate the conditions prior to potential formation of damage and subsequent healing.

In Section 2, we present a derivation of the multicomponent diffusion equations, the effect of stresses-driven diffusion and the evaluation of the CALPHAD-informed diffusion coefficients. In Section 3, the phase-field based RVE is discussed, the crystal plasticity model is briefly presented as well as the diffusion model parameters. We used two RVEs in this study, a simple honeycomb RVE to investigate the role of relative diffusivity of Au and Fe on the cross diffusion in Section 4.1. Then we use a more realistic RVE to evaluate the effect of far-field stress on the accumulation of Au, and thus, its potential for self-healing.

2. Computational methodology

2.1. Binary diffusion model

We start from the generalized flux J_i in a multi-component system with number of components N [34]

$$J_i = -\sum_{j=1}^{N} L_{ij} \nabla \boldsymbol{\Phi}_i \tag{1}$$

where L_{ij} is the phenomenological mobility coefficients and $\boldsymbol{\Phi}_j$ is the diffusion potential. In this work $N = 3$ (Fe, Au and Va). The effect of mechanical stresses on the diffusion of component i is represented by the hydrostatic stress $P = \frac{-\sigma_{ii}}{3}$ in the diffusion potential as

$$\boldsymbol{\Phi}_i = \mu_i + \Delta V_{\text{m}} P \tag{2}$$

where μ_i is the chemical potential of component i and ΔV_{m} is the dilation due to the diffusion of component i. Substituting Eq. (2) in Eq. (1) and making use of $L_{ij} = 0$ for $i \neq j$ [37]

$$J_i = -L_{ii} \nabla \left[\sum_{j=1}^{N} \mu_i + \Delta V_{\text{m}} P \right] \tag{3}$$

For simplicity $\Delta V_{\text{m}} = V_{\text{m}}$ and the molar volume is the same for all components. When the diffusion occurs by the vacancy exchange mechanism, and the vacancies (Va) are chosen as the independent component, then

$$\begin{aligned} J_i &= -L_{ii} \nabla \left[\sum_{j=1}^{N-1} \left(\mu_i - \mu_{\text{Va}} \right) + \Delta V_{\text{m}} P \right] \\ &= -L_{ii} \left[\sum_{j=1}^{N-1} \left(\frac{\partial \mu_i}{\partial x_j} \nabla x_j - \frac{\partial \mu_{\text{Va}}}{\partial x_{\text{Va}}} \nabla x_{\text{Va}} \right) + V_{\text{m}} \nabla P \right] \end{aligned} \tag{4}$$

where x_i is the mole fraction of component i. Using $L_{ii} = \frac{M_i x_i}{V_m}$ where M_i is the mobility of component i, the multicomponent diffusion equation is finally

$$J_i = -\frac{M_i x_i}{V_m}\left[\sum_{j=1}^{N-1}\left(\frac{\partial \mu_i}{\partial x_j}\nabla x_j - \frac{\partial \mu_{\mathrm{Va}}}{\partial x_{\mathrm{Va}}}\nabla x_{\mathrm{Va}}\right) + V_{\mathrm{m}}\nabla P\right] \tag{5}$$

Therefore, the diffusion coefficients are

$$D_{ij} = M_i x_i \frac{\partial \mu_i}{\partial x_j} \tag{6}$$

The non-equilibrium vacancy flux can then be calculated from

$$J_{\mathrm{Va}} = -\sum_{i=1}^{N-1} J_i \tag{7}$$

And finally from the mass conservation with GBs as infinite Va sources/sinks [38]

$$\frac{\partial x_i}{\partial t} = -\nabla \cdot J_i + f_{\mathrm{Va}}^{\mathrm{gb}} \tag{8}$$

Following [39], the strength of the source/sink term $f_{\mathrm{Va}}^{\mathrm{gb}}$ is a function of the local hydrostatic stress and position as will be described next.

2.2. CALPHAD-informed diffusion parameters

The terms $\partial \mu_i / \partial x_j$ = in Eq. (5) are the thermodynamic factors $\Omega_{ij} = \partial^2 G / \partial x_i \partial x_j$ and could be calculated once an expression of the Gibbs free energy G is available, which is of the form [40]

$$G = \sum_i x_i {}^{\circ}G_i + G^{\mathrm{ideal}} + G^{\mathrm{excess}} \tag{9}$$

where ${}^{\circ}G_i$ is the Gibbs free energy of pure component i, G^{ideal} is the entropy of mixing for ideal solution and G^{excess} is the excess term. Such information can be readily obtained from CALPHAD databases. However, such databases seldom contain information on thermal vacancies, which is crucial for evaluating the contribution of vacancies and non-equilibrium vacancy flux in Eqs. (5) and (7) respectively. The treatment of thermal vacancies in the compound energy formalism has been discussed in [41,42]; however, this will require the development of new databases. For a single sublattice and by assuming that vacancies interact ideally with all components, existing databases can be used by adding the vacancy contribution to the RHS of Eq. (9) as

$$G = \sum_{i \neq \mathrm{Va}} x_i {}^{\circ}G_i + G^{\mathrm{ideal}} + G^{\mathrm{excess}} + x_{\mathrm{Va}} {}^{\circ}G_{\mathrm{Va}}^{\mathrm{f}} + RT x_{\mathrm{Va}} \ln(x_{\mathrm{Va}}) \tag{10}$$

where ${}^{\circ}G_{\mathrm{Va}}^{\mathrm{f}}$ is the free energy vacancy formation, R is the universal gas constant and T is the temperature. It should be noted that Eq. (10) is applied only when $x_{\mathrm{Va}} \ll 1$. The term $\partial \mu_{\mathrm{Va}} / \partial x_{\mathrm{Va}}$ can be calculated as

$$\frac{\partial \mu_{\mathrm{Va}}}{\partial x_{\mathrm{Va}}} = \frac{\partial^2 G}{\partial x_{\mathrm{Va}}^2} = \frac{RT}{x_{\mathrm{Va}}} \tag{11}$$

Furthermore, the pressure dependence on the equilibrium vacancy concentration $x_{\mathrm{Va}}^{\mathrm{eq}}$ is [34]

$$x_{\mathrm{Va}}^{\mathrm{eq}} = \exp\left(-\frac{{}^{\circ}G_{\mathrm{Va}}^{\mathrm{f}} + V_{\mathrm{m}} P}{RT}\right) \tag{12}$$

The mobility of the element M_i, neglecting the ferromagnetic effect, could be expressed as [37]

$$M_i = \frac{1}{RT}\exp\left(\frac{-Q_i + RT\ln(M_i^{\circ})}{RT}\right) \tag{13}$$

where Q_i is an activation enthalpy and M_i° is a frequency factor.

3. Model setup

3.1. RVE generation

To understand the effect of microstructure and micromechanical stresses on the multicomponent diffusion model presented in the previous section, a RVE is used. We used the multiphase-field method of Steinbach et al. [43,44] with using only interface energy in the free energy functional to represent grain growth as

$$F = \int_{\Omega} f^{\mathrm{intf}} d\Omega \tag{14}$$

where f^{intf} is the interface free energy density, which is given by

$$f^{\mathrm{intf}} = \sum_{\alpha,\beta,\alpha\neq\beta}^{N} \frac{4\sigma_{\alpha\beta}}{\eta}\left(-\frac{\eta^2}{\pi^2}\nabla\phi_\alpha \cdot \nabla\phi_\beta + \phi_\alpha\phi_\beta\right) \tag{15}$$

where ϕ is the phase-field order parameter representing a grain, $\sigma_{\alpha\beta}$ is the interface energy between phases α and β and η is the interface width. The evolution of ϕ, i.e. microstructure, is given by

$$\dot{\phi} = \frac{\pi^2}{8\eta}\sum_{\alpha\neq\beta}^{N}\frac{\mu_{\alpha\beta}}{N}\left(\frac{\delta F}{\delta \phi_\alpha} - \frac{\delta F}{\delta \phi_\beta}\right) \tag{16}$$

where $\mu_{\alpha\beta}$ is the interface mobility between phases α and β. We developed two RVEs, one is a honeycomb structure (100 × 100 grid points) to simplify the understanding of the model behavior and the second one is a more complex polycrystalline RVE (200 × 200 grid points) to represent a real single phase microstructure as discussed in Sections 4.1 and 4.2 respectively. In all the phase-field grain growth RVEs, an isotropic interface energy of 0.5 J m^{-2}, interface mobility of 1×10^{-14} m^2 J^{-1} s^{-1} and grid spacing Δx of 1 μm. We used the software OpenPhase [45] for solving Eq. (16).

3.2. Crystal plasticity model

For the micromechanics, we used the phenomenological crystal plasticity model, which is solved using the spectral solver implemented in OpenPhase [46]. We briefly summarize the main equations of the crystal plasticity model as follows. The total deformation gradient $\mathbf{F}$ is decomposed into elastic $\mathbf{F}^*$ and plastic $\mathbf{F}^{\mathrm{p}}$ parts as

$$\mathbf{F} = \mathbf{F}^* \cdot \mathbf{F}^{\mathrm{p}} \tag{17}$$

The 12 slip systems $\{110\}\langle\bar{1}11\rangle$ are the active slip systems in BCC iron, which in the deformed configuration are given by

$$\begin{aligned} \mathbf{s}^{*\alpha} &= \mathbf{F}^* \cdot \mathbf{s}^{\alpha} \\ \mathbf{m}^{*\alpha} &= \mathbf{m}^{\alpha} \cdot \mathbf{F}^{*-1} \end{aligned} \tag{18}$$

where the slip system α is defined by its slip direction $\mathbf{s}^{\alpha}$ and normal to the slip plane $\mathbf{m}^{\alpha}$ in the initial configuration. The evolution of the slip rate $\dot{\gamma}$ is modeled using the viscoplastic formulation

$$\dot{\gamma}^{\alpha} = \dot{a}_o^{\alpha}\left(\frac{\tau^{\alpha}}{g^{\alpha}}\right)\left|\frac{\tau^{\alpha}}{g^{\alpha}}\right|^{n-1} \tag{19}$$

where $\dot{a}_o^{\alpha}$ is the reference strain on slip system α, τ^{α} is the resolved shear stress and g^{α} is the function describing its current strength. τ^{α} is expressed as

$$\tau^{\alpha} = \frac{1}{2}(\mathbf{s}^{*\alpha} \otimes \mathbf{m}^{*\alpha} + \mathbf{m}^{*\alpha} \otimes \mathbf{s}^{*\alpha}) : \boldsymbol{\tau} \tag{20}$$

where $\boldsymbol{\tau}$ is the Kirchhoff stress. The evolution of the current strengths g^{α} is given by

$$\dot{g}^{\alpha} = \sum_{\beta} \mathrm{h}_{\alpha\beta}\dot{\gamma}^{\beta} \tag{21}$$

where $\mathrm{h}_{\alpha\beta}$ is the matrix of the hardening moduli. The crystal plasticity parameters are shown in Table 1.

Table 1
Crystal plasticity parameters.

Cubic elasticity constants		Flow and hardening parameters	
C_{11}	236.9 GPa	Reference strain rate $\dot{a}_o$	0.003 s^{-1}
C_{12}	140.6 GPa	Rate sensitivity exponent n	10
C_{44}	116 GPa	Initial critical resolved shear stress τ_o	80 MPa
		Initial hardening modulus h_o	170 MPa
		Saturation stress τ_s	90 MPa
		Ratio of latent to self hardening q	1.1

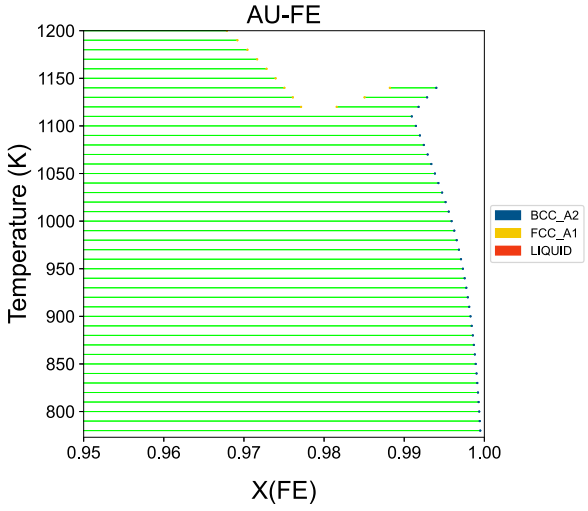

Fig. 1. Phase-diagram of Fe–Au system in the Fe-rich region.

3.3. Diffusion parameters

In this work, we use pycalphad [47] to read the Gibbs free energy and the mobility databases required in Eq. (5), and parse them as SymPy [48] symbolic expressions. This makes it straight forward to calculate the chemical potentials as $\mu_i = \partial G/\partial x_i$, and thus, the thermodynamic factors $\partial\mu_i/\partial x_j$ in Eq. (5). We used the search engine *Thermodynamic DataBase DataBase* [49] to look up the literature for Fe–Au databases that are freely available. The CALPHAD database [50] was used. The phase-diagram in the Fe-rich region is shown in Fig. 1.

The mobility database for Au in BCC Fe was obtained from [51]. For Fe, the temperature dependence of the self-diffusivity D^* was obtained from [52], which could be related to the mobility using $M = \frac{D^*}{RT}$ [40]. The concentration dependence for M_{Fe} and D_{FeFe} is not considered in this study for simplicity. We used a composition of 2% mole fraction of Au at temperature 773 K in BCC iron, i.e. super saturation according to Fig. 1. This was the initial concentration, and was considered uniform along all RVEs. The elemental diffusion coefficients (D_{ii}), both main ($i = j$) and cross-diffusion ($i \neq j$) terms for this composition range and temperature are shown in Fig. 2 according to the aforementioned databases and Eq. (6).

Eq. (5) is solved using the finite-difference method with a 13-point stencil and forward Euler time integration with a time step increment Δt according to the stability criterion $D\Delta t/\Delta x^2 \leq 1/4$. All diffusion simulations were subjected to periodic boundary conditions (see Table 2).

The source/sink term in Eq. (8) were applied to the GB regions that could be identified from the double-well potential of the phase-field based RVE as $\sum_\alpha \sum_{\beta\neq\alpha} \phi_\alpha\phi_\beta$ using Eq. (12), which included the effect of local hydrostatic stress dependency.

4. Results and discussion

4.1. Honeycomb RVE

The morphology of the honeycomb RVE is shown in Fig. 3. In all the simulations, the mechanical loading was first applied monotonically

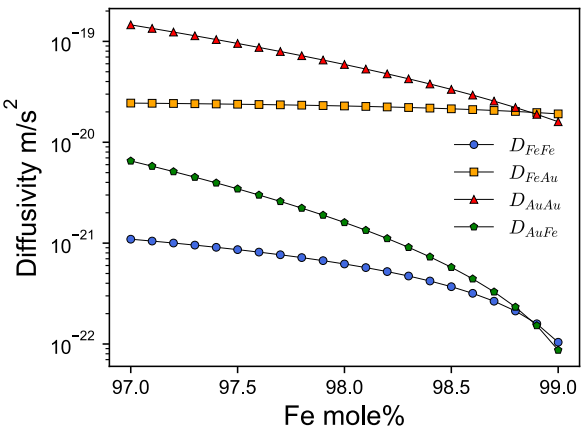

Fig. 2. The main and cross-diffusion coefficients at 773 K.

Table 2
Parameters used in the simulation.

Parameter	Value
V_m (m^3/mol)	7.09×10^{-6}
T (K)	773
R (J/molK)	8.31
$^\circ G^f_{Va}$ (kJ/mol)	77.17

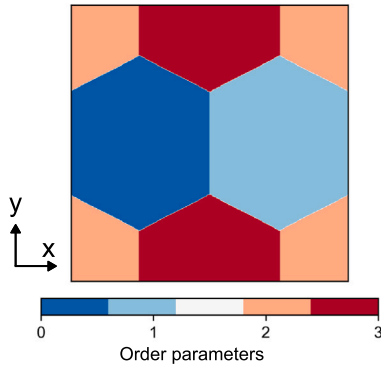

Fig. 3. The order parameters representing the honeycomb RVE.

up to a designated stress, then the diffusion calculation was performed according to Eq. (5). A 100 MPa load was applied in the $x-$direction of Fig. 3, perpendicular to the GB in the middle of the RVE, with periodic boundary conditions. The hydrostatic stress distribution and the corresponding equilibrium vacancy concentration is shown in Fig. 4. It can be seen that the maximum tensile hydrostatic stresses are at the GBs perpendicular to the loading direction. Consequently, the equilibrium vacancy concentration, following Eq. (12), will have its maximum at the regions with maximum tensile hydrostatic stress.

The corresponding concentration fields of Fe and Au are shown in Fig. 5. It can be seen that the redistribution of Au follows the same pattern as the hydrostatic stress in Fig. 4(a) where the regions of higher tensile hydrostatic stresses, i.e. the regions that are likely to nucleate voids, have higher Au concentrations compared to the less tensile/compressive ones. This is due to the hydrostatic stress gradient driving force in Eq. (5) which enriches the regions of higher tensile hydrostatic stress and depletes those with a lower tensile hydrostatic stress.

On the other side, the redistribution of Fe shows the opposite pattern to that of Au, i.e. the more tensile regions have less Fe that the

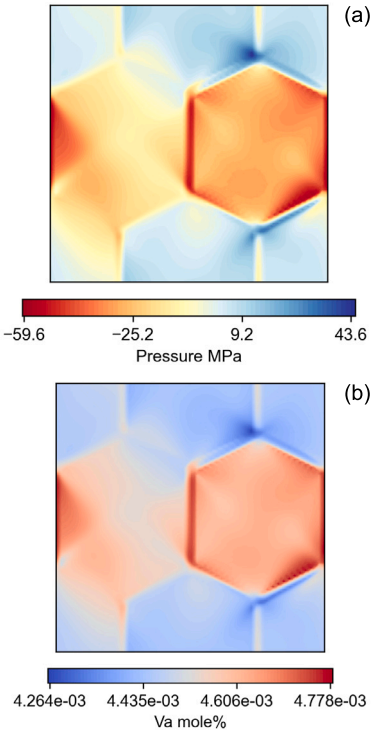

Fig. 4. (a) The hydrostatic stress distribution resulting from a far-field 100 MPa in the horizontal direction and (b) corresponding equilibrium vacancy concentration.

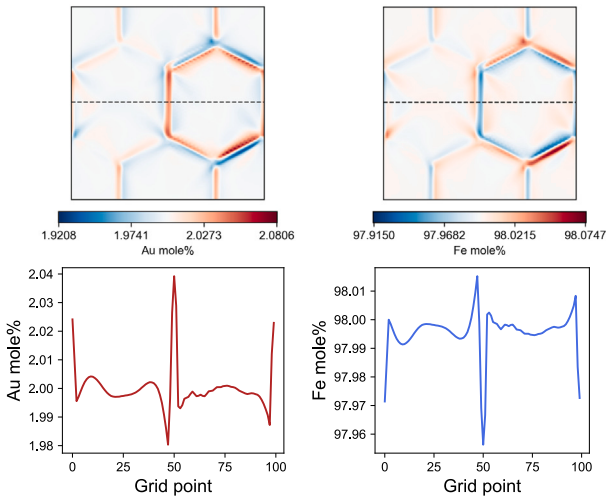

Fig. 5. The stress-driven redistribution of Au and Fe. The dashed lines are the locations of line profiles.

less tensile ones. This is despite that Fe is also subjected to the same hydrostatic stress gradient driving force as Au. This is due to the cross diffusion terms in Eq. (5) where the flux of Fe is not only affected by the concentration gradient of Fe, but also due the concentration gradient of Au. Therefore, the enrichment of Au in the high tensile regions develops a driving force that drives Fe towards the less tensile ones.

However, Au should be subjected to the same cross diffusion from Fe. The decisive factor that determines which element will diffuse towards the highly tensile regions is its relative diffusivity. Since $D_{AuAu} > D_{FeFe}$ as in Fig. 2, Au is faster and diffuses towards the tensile regions, developing Fe flux in the opposite direction. To test this hypothesis, we run a simulation with artificially increasing D_{FeFe} tenfold, resulting in

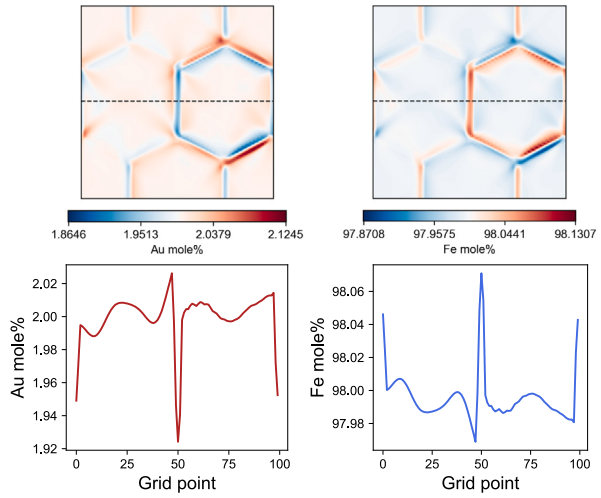

Fig. 6. The stress-driven redistribution of Au and Fe when D_{FeFe} is artificially increased by a factor of 10. The dashed lines are the locations of line profiles.

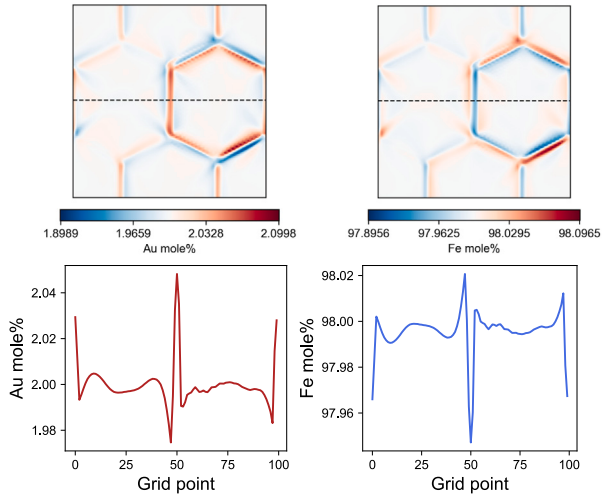

Fig. 7. The stress-driven redistribution of Au and Fe when D_{AuAu} is artificially increased by a factor of 10. The dashed lines are the locations of line profiles.

$D_{FeFe} > D_{AuAu}$. Indeed, as shown in Fig. 6, we can see in this hypothetical case that the behavior is reversed where Fe diffuses towards the highly tensile regions, while Au diffuses towards the less tensile ones. Additionally, we also increase D_{AuAu} tenfold compared to Fig. 2. It could be seen in Fig. 7 that this resulted in a further enrichment, although only slightly, of Au in the higher tensile regions and more depletion in the lower tensile/compressive regions compared to Fig. 5.

Since the highly tensile regions are mainly near GBs, they act as vacancy sources. According to the classical nucleation theory of Raj and Ashby [53,54], a high concentration of vacancies will condense into a nano void, which is assisted by the presence of secondary particles and interfaces [55], i.e. heterogeneous nucleation. These voids will only grow in the tensile regions. This is essentially similar to stress voiding in metallic interconnects [56]. Because of stress-driven diffusion, Au will accumulate in these tensile regions, further increasing the local supersaturation. As discussed earlier, an essential condition is $D_{AuAu} > D_{FeFe}$. The open volume of voids will then allow Au to nucleate and precipitate, preventing the voids from further growing, and thus, healing them.

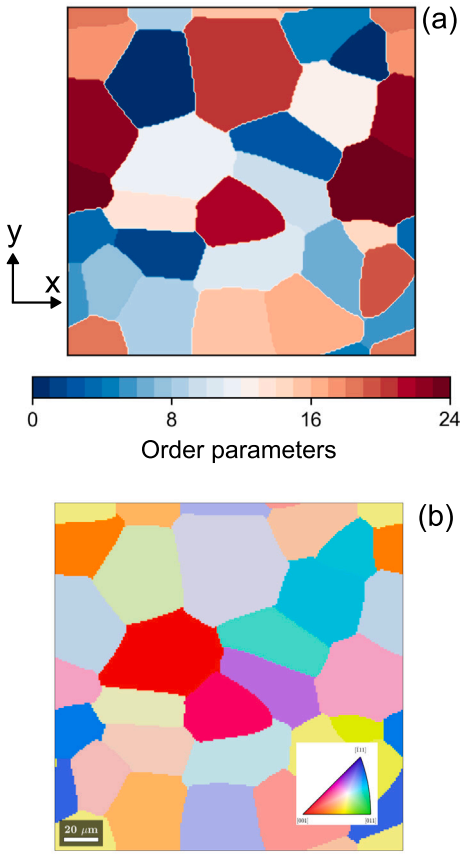

Fig. 8. 2D Polycrystalline RVE (a) phase-field order parameters ϕ_i representing the morphology of the grains and (b) orientation map.

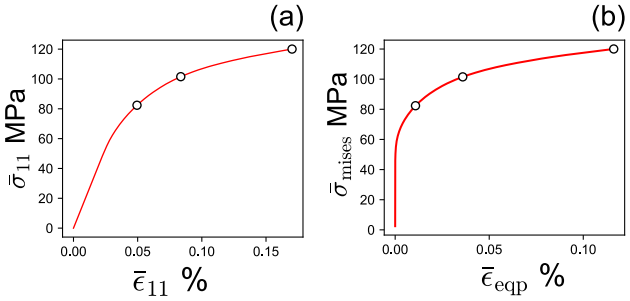

Fig. 9. The averaged stress–strain curves showing the three selected stress points for performing diffusion simulations for the polycrystalline RVE.

4.2. 2D polycrystalline RVE

In this section, we investigate the effect of stress on the redistribution of Au and Fe in a more complex polycrystalline RVE. The RVE is shown in Fig. 8(a) and the corresponding orientation map in Fig. 8(b). The RVE is subjected to a monotonically increasing tensile stress in the x−direction of Fig. 8. The stress–strain curve is shown in Fig. 9. We selected three points at 80, 100 and 120 MPa to investigate the effect of increasing stress on Au diffusion and vacancy concentration.

The distribution of hydrostatic stress as a result of the far-field stress is shown in the first row of Fig. 10. It could be seen that the regions with the highest hydrostatic stress are mostly at the GBs and/or triple junctions that are perpendicular to or slightly misaligned with the loading direction. As expected, increasing the far-field stress, the maximum stress levels in the highly stressed regions. The stress triaxiality, calculated as $-P/\sigma_{\text{mises}}$ is shown in the second row. The regions with high triaxiality, in general, have high tensile hydrostatic stress. The equilibrium vacancy concentration is shown in the third row of Fig. 10. Again, according to Eq. (12), the highly tensile regions have the highest vacancy concentration, and thus are potential sites for void nucleation and growth.

The distribution of Au and Fe is shown in Figs. 11 and 12 respectively. As described before, Au diffuses towards the highly tensile regions due to the stress driving force. The high diffusivity of Au allows it to diffuse faster than Fe towards these regions and build up, developing flux of Fe towards the less tensile regions. Increasing the far-field stress increases the enrichment of Au in the tensile regions as well as the depletion from the less tensile ones.

As discussed in the previous section, the high tensile stresses develop at GBs mainly perpendicular to the loading direction. The increased vacancy concentration in these regions means a higher tendency for void growth. Indeed, it was shown that increasing the stress increases the fraction of voids [18]. Fig. 11 also shows increased local Au concentration at the most highly loaded grain boundaries. From this, one might expect an increase in self-healing behavior with increasing externally applied stress. However, it has been reported that stresses above a certain level lead to a reduction in the number of completely or partially filled voids, i.e. a reduced healing efficiency, decrease [18].

This behavior might be attributed to the competition between the kinetics of void growth and Au precipitation. It was shown that increased stress triaxiality leads to void growth and coalescence [56,57]. Indeed, Fig. 10 shows increased stress triaxiality with increasing the stress. This will result in additional driving force to void growth in addition to the increased vacancy concentration, while the increased Au transport is not sufficient enough to heal the growing voids. This motivates the need for a complete theoretical analysis of the kinetics of void formation and precipitation of the Au solute atoms therein. However, this is beyond the scope of the current work, which focused on the pre-conditioning of the material before the occurrence of both processes.

5. Conclusions

In this work, we investigated the role of cross-diffusion and stress-driven diffusion on the Fe–Au system in order to provide more understanding of the prior conditions of the creep-void growth and self-healing observed in this class of alloys. The diffusion coefficients were obtained using CALPHAD databases. RVE and crystal plasticity model were used to evaluate the role of microstructure heterogeneities. The following conclusions can be made:

- High tensile hydrostatic stresses develop mainly at GBs and triple junctions perpendicular to loading direction. Equilibrium vacancy concentration are also maximum at these regions. Therefore, these are expected to be the void nucleation and growth as observed experimentally.
- Fe and Au have stress driving force to diffuse towards these highly tensile regions from the less tensile ones. However, cross diffusion plays a crucial role in determining which of Fe or Au will enrich the highly tensile regions. The essential condition for this is the relative diffusivity. Since $D_{AuAu} > D_{FeFe}$ will enrich the highly tensile regions, increasing the potential of precipitation and self-healing.
- Increasing the far-field stress, increases the tensile hydrostatic stress at the GB regions as well as both Vacancy and Au enrichment. However, this also leads to increased stress triaxiality. This is expected to increase void growth rate, and thus, decrease the self-healing efficiency.

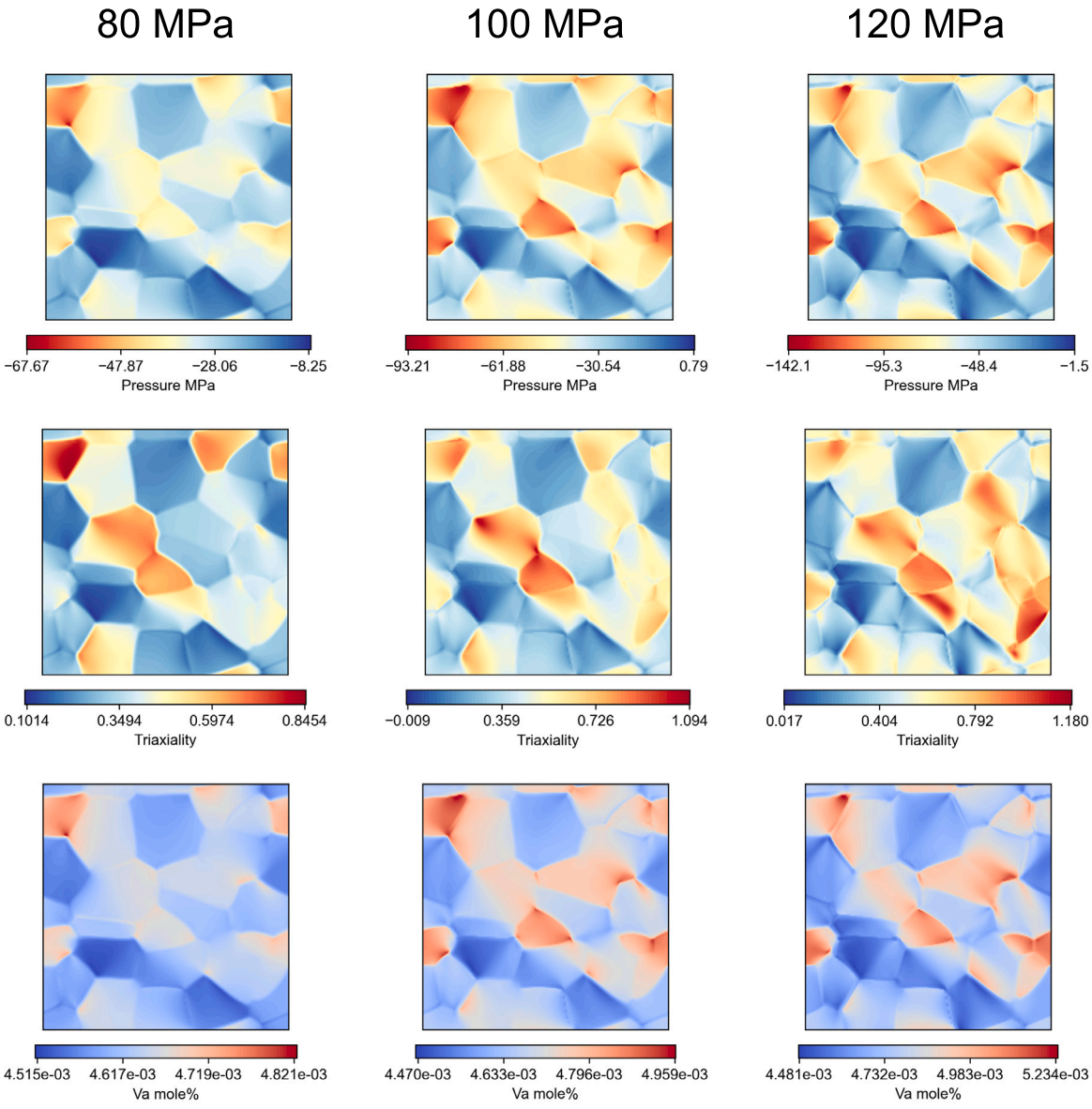

Fig. 10. The effect of far-field stress on the hydrostatic stress distribution in the first row. The corresponding stress triaxiality in the second row. The equilibrium vacancy concentration in the third row.

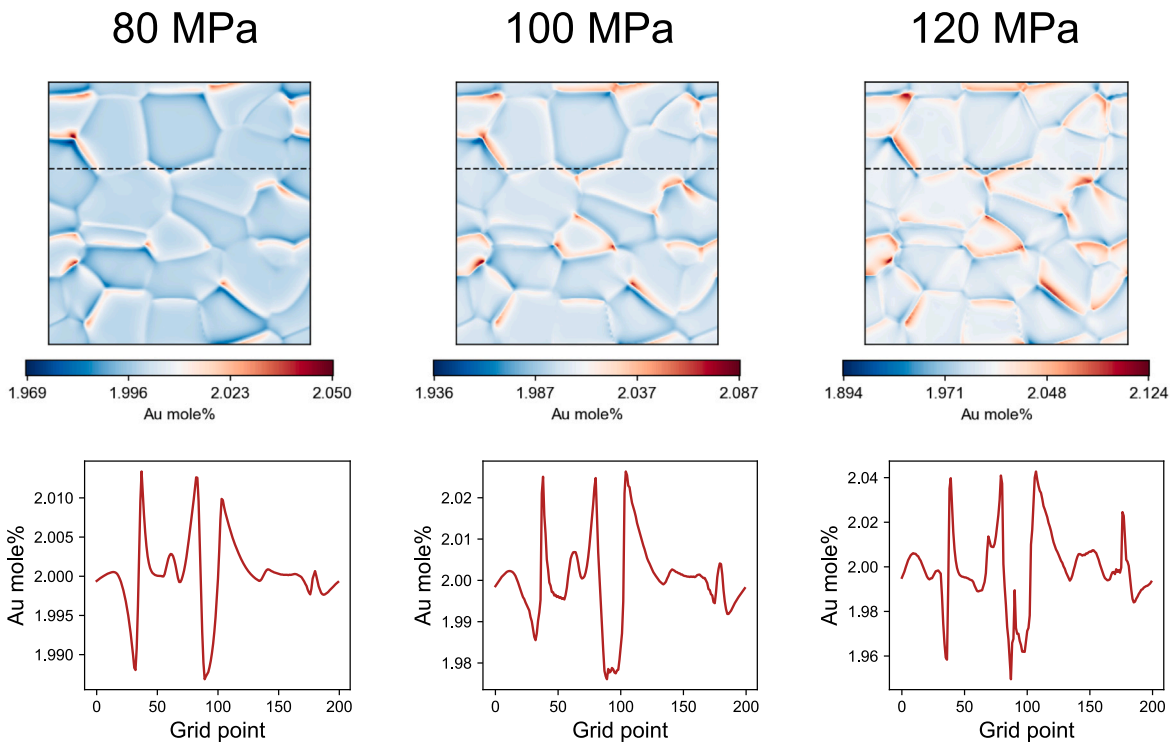

Fig. 11. The effect of increasing the far-field stress on the local Au distribution.

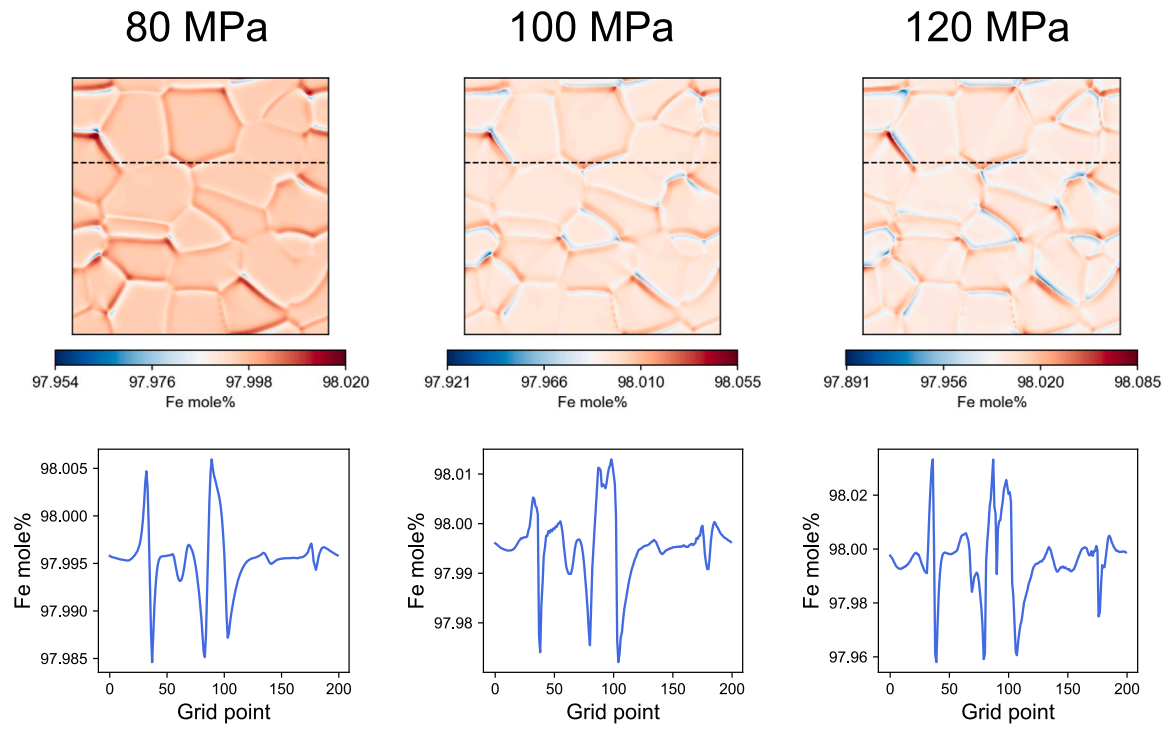

Fig. 12. The effect of increasing the far-field stress on the local Fe distribution.

CRediT authorship contribution statement

Abdelrahman Hussein: Conceptualization, Methodology, Software, Writing – original draft. **Sybrand van der Zwaag:** Writing – review & editing, Conceptualization, Methodology, Supervision. **Byungki Kim:** Funding acquisition, Supervision, Writing – review & editing, Conceptualization, Methodology.

Declaration of competing interest

The authors declare that they have no known competing financial interests or personal relationships that could have appeared to influence the work reported in this paper.

Data availability

Data will be made available on request.

Acknowledgments

This work was supported by the National Research Foundation of Korea (NRF) by grant NRF-2018R1A6A1A03025526 of the Priority Research Program under the Ministry of Education, and in part by grant NRF-2021R1A2C1004540 under the Ministry of Science and ICT.

References

[1] M. Ashby, B. Dyson, Creep damage mechanics and micromechanisms, in: Fracture 84, Elsevier, 1984, pp. 3–30, http://dx.doi.org/10.1016/b978-1-4832-8440-8.50017-x.
[2] A. Cocks, M. Ashby, On creep fracture by void growth, Prog. Mater. Sci. 27 (3–4) (1982) 189–244, http://dx.doi.org/10.1016/0079-6425(82)90001-9.
[3] A. Cocks, A. Searle, Void growth by grain-boundary diffusion in fine grained materials, Mech. Mater. 12 (3–4) (1991) 279–287, http://dx.doi.org/10.1016/0167-6636(91)90024-t.
[4] C. Gandhi, R. Raj, Intergranular fracture in bicrystals–II, Acta Metall. 30 (2) (1982) 505–511, http://dx.doi.org/10.1016/0001-6160(82)90231-0.
[5] P. Shewmon, P. Anderson, Void nucleation and cracking at grain boundaries, Acta Mater. 46 (14) (1998) 4861–4872, http://dx.doi.org/10.1016/s1359-6454(98)00194-3.
[6] J.-D. Hu, F.-Z. Xuan, C.-J. Liu, A void growth model of multiaxial power-law creep rupture involving the void shape changes, Int. J. Mech. Sci. 144 (2018) 723–730, http://dx.doi.org/10.1016/j.ijmecsci.2018.05.011.
[7] Q. Lu, W. Xu, S. van der Zwaag, Designing new corrosion resistant ferritic heat resistant steel based on optimal solid solution strengthening and minimisation of undesirable microstructural components, Comput. Mater. Sci. 84 (2014) 198–205, http://dx.doi.org/10.1016/j.commatsci.2013.12.009.
[8] Q. Lu, Y. Toda, N. Harada, W. Xu, S. van der Zwaag, The impact of intended service temperature on the optimal composition of laves and M23C6 precipitate strengthened ferritic creep resistant steels, Comput. Mater. Sci. 107 (2015) 110–115, http://dx.doi.org/10.1016/j.commatsci.2015.05.016.
[9] M. Shu, Q. Zhou, Y. Shen, Z. Zhou, P. Wang, L. Chen, Y. Sun, J. Xiao, Improved creep resistance of 20Cr25NiNb heat resistant steels through grain boundary intermetallic precipitation strengthening, J. Mater. Res. Technol. 25 (2023) 3728–3743, http://dx.doi.org/10.1016/j.jmrt.2023.06.213.
[10] M. Akhtar, A. Khajuria, Effects of prior austenite grain size on impression creep and microstructure in simulated heat affected zones of boron modified P91 steels, Mater. Chem. Phys. 249 (2020) 122847, http://dx.doi.org/10.1016/j.matchemphys.2020.122847.
[11] S. van der Zwaag (Ed.), Self Healing Materials, Springer Netherlands, 2007, http://dx.doi.org/10.1007/978-1-4020-6250-6.
[12] A. Kumthekar, S.A. Ponnusami, S. van der Zwaag, S. Turteltaub, Uncertainty quantification of the lifetime of self-healing thermal barrier coatings based on surrogate modelling of thermal cyclic fracture and healing, Mater. Des. 221 (2022) 110973, http://dx.doi.org/10.1016/j.matdes.2022.110973.
[13] M. Arseenko, F. Hannard, L. Ding, L. Zhao, E. Maire, J. Villanova, H. Idrissi, A. Simar, A new healing strategy for metals: Programmed damage and repair, Acta Mater. 238 (2022) 118241, http://dx.doi.org/10.1016/j.actamat.2022.118241.
[14] S.P. Pasaribu, I. Masmur, Hestina, A.S. Panggabean, Facile synthesis of self-healing poly-acrylic acid/TiO2 hybrid hydrogel for photocatalytic hydrogenation of 4-nitrophenol to 4-aminophenol, Mater. Chem. Phys. 305 (2023) 127875, http://dx.doi.org/10.1016/j.matchemphys.2023.127875.
[15] T. Peng, J. Huang, Z. Gong, X. Chen, Y. Chen, Self-healing of reversibly cross-linked thermoplastic vulcanizates, Mater. Chem. Phys. 292 (2022) 126804, http://dx.doi.org/10.1016/j.matchemphys.2022.126804.
[16] A.R. Simbar, A. Shanaghi, H. Moradi, P.K. Chu, Corrosion behavior of functionally graded and self-healing nanostructured TiO2–Al2O3 - benzotriazole coatings deposited on AA 2024-T3 by the sol-gel method, Mater. Chem. Phys. 240 (2020) 122233, http://dx.doi.org/10.1016/j.matchemphys.2019.122233.
[17] N. van Dijk, S. van der Zwaag, Self-healing phenomena in metals, Adv. Mater. Interfaces 5 (17) (2018) 1800226, http://dx.doi.org/10.1002/admi.201800226.
[18] S. Zhang, C. Kwakernaak, W. Sloof, E. Brück, S. van der Zwaag, N. van Dijk, Self healing of creep damage by gold precipitation in iron alloys, Adv. Eng. Mater. 17 (5) (2015) 598–603, http://dx.doi.org/10.1002/adem.201400511.
[19] H. Fang, C. Versteylen, S. Zhang, Y. Yang, P. Cloetens, D. Ngan-Tillard, E. Brück, S. van der Zwaag, N. van Dijk, Autonomous filling of creep cavities in Fe-Au alloys studied by synchrotron X-ray nano-tomography, Acta Mater. 121 (2016) 352–364, http://dx.doi.org/10.1016/j.actamat.2016.09.023.
[20] S. Zhang, H. Fang, M.E. Gramsma, C. Kwakernaak, W.G. Sloof, F.D. Tichelaar, M. Kuzmina, M. Herbig, D. Raabe, E. Brück, S. van der Zwaag, N.H. van Dijk, Autonomous filling of grain-boundary cavities during creep loading in Fe-Mo alloys, Metall. Mater. Trans. A 47 (10) (2016) 4831–4844, http://dx.doi.org/10.1007/s11661-016-3642-0.
[21] H. Fang, N. Szymanski, C. Versteylen, P. Cloetens, C. Kwakernaak, W. Sloof, F. Tichelaar, S. Balachandran, M. Herbig, E. Brück, S. van der Zwaag, N. van Dijk, Self healing of creep damage in iron-based alloys by supersaturated tungsten, Acta Mater. 166 (2019) 531–542, http://dx.doi.org/10.1016/j.actamat.2019.01.014.
[22] Y. Fu, C. Kwakernaak, W.G. Sloof, F.D. Tichelaar, E. Brück, S. van der Zwaag, N.H. van Dijk, Competitive healing of creep-induced damage in a ternary Fe-3Au-4W alloy, Metall. Mater. Trans. A 51 (9) (2020) 4442–4455, http://dx.doi.org/10.1007/s11661-020-05862-6.
[23] Y. Fu, H. Fang, F. Monaco, P. Cloetens, F. Tichelaar, J. van Meel, E. Brück, S. van der Zwaag, N. van Dijk, Self healing of creep-induced damage in Fe-3Au-4W by multiple healing agents studied by synchrotron X-ray nano-tomography, Acta Mater. 239 (2022) 118266, http://dx.doi.org/10.1016/j.actamat.2022.118266.
[24] C.D. Versteylen, M.H.F. Sluiter, N.H. van Dijk, Modelling the formation and self-healing of creep damage in iron-based alloys, J. Mater. Sci. 53 (20) (2018) 14758–14773, http://dx.doi.org/10.1007/s10853-018-2666-9.
[25] C.D. Versteylen, N.H. van Dijk, M.H.F. Sluiter, First-principles analysis of solute diffusion in dilute bcc Fe-X alloys, Phys. Rev. B 96 (9) (2017) 094105, http://dx.doi.org/10.1103/physrevb.96.094105.
[26] Y. Qi, G. Richter, E. Suadiye, M. Kalina, E. Rabkin, Plastic forming of metals at the nanoscale: Interdiffusion-induced bending of bimetallic nanowhiskers, ACS Nano 14 (9) (2020) 11691–11699, http://dx.doi.org/10.1021/acsnano.0c04327.
[27] S. Zhang, C. Kwakernaak, F.D. Tichelaar, W.G. Sloof, M. Kuzmina, M. Herbig, D. Raabe, E. Brück, S. van der Zwaag, N.H. van Dijk, Autonomous repair mechanism of creep damage in Fe-Au and Fe-Au-B-N alloys, Metall. Mater. Trans. A 46 (12) (2015) 5656–5670, http://dx.doi.org/10.1007/s11661-015-3169-9.
[28] H. Yu, W. Xu, S. van der Zwaag, A first step towards computational design of W-containing self-healing ferritic creep resistant steels, Sci. Technol. Adv. Mater. 21 (1) (2020) 641–652, http://dx.doi.org/10.1080/14686996.2020.1814679.
[29] Y. Fu, C. Kwakernaak, J.C. Brouwer, W.G. Sloof, E. Brück, S. van der Zwaag, N.H. van Dijk, Surface precipitation of supersaturated solutes in a ternary Fe–Au–W alloy and its binary counterparts, J. Mater. Sci. 56 (8) (2020) 5173–5189, http://dx.doi.org/10.1007/s10853-020-05571-w.
[30] C.D. Versteylen, N.K. Szymański, M.H.F. Sluiter, N.H. van Dijk, Finite element modelling of creep cavity filling by solute diffusion, Phil. Mag. 98 (10) (2018) 864–877, http://dx.doi.org/10.1080/14786435.2017.1418097.
[31] Y. Fu, S. van der Zwaag, N.H. van Dijk, Modelling the growth and filling of creep-induced grain-boundary cavities in self-healing alloys, J. Mater. Sci. 57 (25) (2022) 12034–12054, http://dx.doi.org/10.1007/s10853-022-07352-z.
[32] H. Bhadeshia, A commentary on: "diffusion of carbon in austenite with a discontinuity in composition", Metall. Mater. Trans. A 41 (7) (2010) 1605–1615, http://dx.doi.org/10.1007/s11661-010-0276-5.
[33] F. Larché, J. Cahn, A linear theory of thermochemical equilibrium of solids under stress, Acta Metall. 21 (8) (1973) 1051–1063, http://dx.doi.org/10.1016/0001-6160(73)90021-7.
[34] R.W. Balluffi, S.M. Allen, W.C. Carter, Kinetics of Materials, Wiley, 2005, http://dx.doi.org/10.1002/0471749311.
[35] R. Fernández-Sousa, C. Betegón, E. Martínez-Pañeda, Analysis of the influence of microstructural traps on hydrogen assisted fatigue, Acta Mater. 199 (2020) 253–263, http://dx.doi.org/10.1016/j.actamat.2020.08.030.
[36] A. Hussein, A.H. Krom, P. Dey, G.K. Sunnardianto, O.A. Moultos, C.L. Walters, The effect of hydrogen content and yield strength on the distribution of hydrogen in steel: a diffusion coupled micromechanical FEM study, Acta Mater. 209 (2021) 116799, http://dx.doi.org/10.1016/j.actamat.2021.116799.
[37] J.-O. Andersson, J. Ågren, Models for numerical treatment of multicomponent diffusion in simple phases, J. Appl. Phys. 72 (4) (1992) 1350–1355, http://dx.doi.org/10.1063/1.351745.
[38] C. Herring, Diffusional viscosity of a polycrystalline solid, J. Appl. Phys. 21 (5) (1950) 437–445, http://dx.doi.org/10.1063/1.1699681.
[39] A. Chakraborty, R.A. Lebensohn, L. Capolungo, Coupled chemo-mechanical modeling of point-defect diffusion in a crystal plasticity fast Fourier transform framework, J. Mech. Phys. Solids 173 (2023) 105190, http://dx.doi.org/10.1016/j.jmps.2022.105190.

[40] U.R. Kattner, C.E. Campbell, Invited review: Modelling of thermodynamics and diffusion in multicomponent systems, Mater. Sci. Technol. 25 (4) (2009) 443–459, http://dx.doi.org/10.1179/174328408x372001.
[41] J. Rogal, S.V. Divinski, M.W. Finnis, A. Glensk, J. Neugebauer, J.H. Perepezko, S. Schuwalow, M.H.F. Sluiter, B. Sundman, Perspectives on point defect thermodynamics, Phys. Status Solidi (b) 251 (1) (2013) 97–129, http://dx.doi.org/10.1002/pssb.201350155.
[42] J. Ågren, M. Hillert, Thermodynamic modelling of vacancies as a constituent, CALPHAD 67 (2019) 101666, http://dx.doi.org/10.1016/j.calphad.2019.101666.
[43] I. Steinbach, Phase-field models in materials science, Modelling Simul. Mater. Sci. Eng. 17 (7) (2009) 073001, http://dx.doi.org/10.1088/0965-0393/17/7/073001.
[44] I. Steinbach, Phase-field model for microstructure evolution at the mesoscopic scale, Annu. Rev. Mater. Res. 43 (1) (2013) 89–107, http://dx.doi.org/10.1146/annurev-matsci-071312-121703.
[45] M. Tegeler, O. Shchyglo, R.D. Kamachali, A. Monas, I. Steinbach, G. Sutmann, Parallel multiphase field simulations with OpenPhase, Comput. Phys. Comm. 215 (2017) 173–187, http://dx.doi.org/10.1016/j.cpc.2017.01.023.
[46] E. Borukhovich, P.S. Engels, J. Mosler, O. Shchyglo, I. Steinbach, Large deformation framework for phase-field simulations at the mesoscale, Comput. Mater. Sci. 108 (2015) 367–373, http://dx.doi.org/10.1016/j.commatsci.2015.06.021.
[47] R. Otis, Z.-K. Liu, Pycalphad: CALPHAD-based computational thermodynamics in python, J. Open Res. Softw. 5 (1) (2017) 1, http://dx.doi.org/10.5334/jors.140.
[48] A. Meurer, C.P. Smith, M. Paprocki, O. Čertík, S.B. Kirpichev, M. Rocklin, A. Kumar, S. Ivanov, J.K. Moore, S. Singh, T. Rathnayake, S. Vig, B.E. Granger, R.P. Muller, F. Bonazzi, H. Gupta, S. Vats, F. Johansson, F. Pedregosa, M.J. Curry, A.R. Terrel, Š. Roučka, A. Saboo, I. Fernando, S. Kulal, R. Cimrman, A. Scopatz, SymPy: symbolic computing in python, PeerJ Comput. Sci. 3 (2017) e103, http://dx.doi.org/10.7717/peerj-cs.103.
[49] A. van de Walle, C. Nataraj, Z.-K. Liu, The thermodynamic database database, CALPHAD 61 (2018) 173–178, http://dx.doi.org/10.1016/j.calphad.2018.04.003.
[50] Y. Liu, Y. Ge, D. Yu, Thermodynamic descriptions for Au–Fe and Na–Zn binary systems, J. Alloys Compd. 476 (1–2) (2009) 79–83, http://dx.doi.org/10.1016/j.jallcom.2008.09.012.
[51] Y. Liu, L. Zhang, Y. Du, D. Liang, Ferromagnetic ordering and mobility end-members for impurity diffusion in bcc Fe, CALPHAD 33 (4) (2009) 732–736, http://dx.doi.org/10.1016/j.calphad.2009.09.007.
[52] Y. Iijima, Y. Yamazaki, Interdiffusion between metals of widely different self-diffusion rates, Defect Diffus. Forum 237–240 (2005) 62–73, http://dx.doi.org/10.4028/www.scientific.net/ddf.237-240.62.
[53] R. Raj, M. Ashby, Intergranular fracture at elevated temperature, Acta Metall. 23 (6) (1975) 653–666, http://dx.doi.org/10.1016/0001-6160(75)90047-4.
[54] F. Meixner, M.R. Ahmadi, C. Sommitsch, Modeling and simulation of pore formation in a bainitic steel during creep, Metall. Mater. Trans. A 53 (3) (2022) 984–999, http://dx.doi.org/10.1007/s11661-021-06569-y.
[55] M. Kassner, Creep fracture, in: Fundamentals of Creep in Metals and Alloys, Elsevier, 2015, pp. 233–260, http://dx.doi.org/10.1016/b978-0-08-099427-7.00010-4.
[56] Z. Suo, Reliability of metal interconnects, in: Comprehensive Structural Integrity, Elsevier, 2003, pp. 265–324, http://dx.doi.org/10.1016/b0-08-043749-4/08125-8.
[57] E.V.D. Giessen, M.V.D. Burg, A. Needleman, V. Tvergaard, Void growth due to creep and grain boundary diffusion at high triaxialities, J. Mech. Phys. Solids 43 (1) (1995) 123–165, http://dx.doi.org/10.1016/0022-5096(94)00059-e.